Acta Crystallographica Section B
**Structural Science**
ISSN 0108-7681

# High-pressure structures of $\alpha$- and $\delta$-$ZrMo_2O_8$

**Anne Marie Krogh Andersen[a] and Stefan Carlson[b]*†**

[a]Department of Chemistry, Odense University, DK-5230 Odense M, Denmark, and [b]European Synchrotron Radiation Facility (ESRF), BP 220, F-38043 Grenoble CEDEX, France

† Present address: MAX-lab, Lund University, Box 118, SE-22100 Lund, Sweden.

Correspondence e-mail: stefan.carlson@maxlab.lu.se

Received 11 September 2000
Accepted 26 September 2000

*In situ* high-pressure synchrotron X-ray powder diffraction studies of trigonal $\alpha$-$ZrMo_2O_8$, zirconium molybdate, have been performed from ambient conditions to 1.9 GPa, over the $\alpha$–$\delta$ phase transition at 1.06–1.11 GPa. The monoclinic structure of $\delta$-$ZrMo_2O_8$, stable between 1.1 and 2.5 GPa at 298 K, has been solved by direct methods and refined using the Rietveld method. Significant distortions of the $ZrO_6$ and $MoO_4$ polyhedral elements are observed for $\delta$-$ZrMo_2O_8$, as compared to the ambient conditions of the $\alpha$-phase, while the packing of anions becomes more symmetric at high pressure.

## 1. Introduction

Over the last few decades investigations on $MX_2O_8$ and $MX_2O_7$ compounds ($M$ = Zr, Ti, Hf and $X$ = P, V, Mo, W) have revealed a large number of intriguing framework structures. Especially the isotropic negative thermal expansion properties of *e.g.* $ZrW_2O_8$ (Mary *et al.*, 1996), $HfW_2O_8$ (Evans *et al.*, 1996), $ZrV_2O_7$ (Korthuis *et al.*, 1995) and cubic $ZrMo_2O_8$ (Lind *et al.*, 1998) indicate that these types of compounds may have important technological applications in *e.g.* composites with specific properties (Chu *et al.*, 1987). Also trigonal $ZrMo_2O_8$ has been shown to display highly anisotropic thermal expansion coefficients with a slightly negative expansion for the *a* axis and strongly positive for the *c* axis (Mittal *et al.*, 1999). Investigations of zirconium molybdates and basic zirconium molybdate have also been performed owing to their possible use as catalysts (Prinetto *et al.*, 1995), ion-exchangers (Clearfield & Blessing, 1972), luminescence (Blasse & Dirksen, 1987) and in nuclear fuel processes (Pankajavalli & Sreedharan, 1990; Adachi *et al.*, 1988). Studies of these compounds at ambient conditions as well as elevated temperatures are numerous, while investigations at high pressures are fairly scarce.

Comprehensive studies on the high-pressure properties of $ZrW_2O_8$ have previously been performed, showing a transition from cubic $\alpha$-$ZrW_2O_8$ to orthorhombic $\gamma$-$ZrW_2O_8$ at 0.21 GPa (Evans *et al.*, 1997; Jorgensen *et al.*, 1999), and amorphization progressively from 1.5 to 3.5 GPa (Perottoni & Jordana, 1998). High-pressure studies up to 0.6 GPa have also been performed on cubic $\gamma$-$ZrMo_2O_8$ (Lind *et al.*, 1998). Recently, we reported two reversible high-pressure phase transitions for $\alpha$-$ZrMo_2O_8$ from trigonal to monoclinic ($\delta$-$ZrMo_2O_8$) and from monoclinic to triclinic ($\varepsilon$-$ZrMo_2O_8$) symmetries at 1.06–1.11 and 2.0–2.5 GPa, respectively (Carlson & Krogh Andersen, 2000). It was shown that the volume compressibilities are similar for the $\alpha$- and $\delta$-phases, which in turn are five times lower for the triclinic $\varepsilon$-phase.

Several different polymorphs of $ZrMo_2O_8$ have previously been reported in the literature: cubic ($\gamma$-$ZrMo_2O_8$; Lind *et al.*,

1998), trigonal ($\alpha$-$ZrMo_2O_8$; Auray *et al.*, 1986; Serezhkin *et al.*, 1987) and monoclinic ($\beta$-$ZrMo_2O_8$; Klevtsova *et al.*, 1989; Auray *et al.*, 1987; Auray *et al.*, 1989). The metastable structure of $\gamma$-$ZrMo_2O_8$ ($a$ = 9.13 Å, space group $Pa\bar{3}$) transforms completely to $\alpha$-$ZrMo_2O_8$ ($a$ = 10.14 and $c$ = 11.70 Å, space group $P\bar{3}1c$) upon longer heating times at 663 K, while the direct transformation to the thermodynamically more stable low-temperature form $\beta$-$ZrMo_2O_8$ ($a$ = 11.43, $b$ = 7.94, $c$ = 7.46 Å and $\beta$ = 122.3°, space group $C2/c$) seems to be kinetically controlled (Lind *et al.*, 1998).

The structure of $\alpha$-$ZrMo_2O_8$ was solved from single-crystal data by Auray *et al.* (1986) and Serezhkin *et al.* (1987). It is a two-dimensional network with layers perpendicular to the $c$ axis. The layers are built from $ZrO_6$ octahedra linked together by $MoO_4$ tetrahedra. Each tetrahedral molybdate group is linked *via* three of the O atoms to three different zirconium atoms. The fourth oxygen in the $MoO_4$ tetrahedron points into the interlayer region. The only isostructural compound to $\alpha$-$ZrMo_2O_8$ is $HfMo_2O_8$ (Rimsky *et al.*, 1968), but they show topological similarities with *e.g.* glaserite $K_3Na(SO_4)_2$ (Moore, 1973). In fact, $\alpha$-$ZrMo_2O_8$ can be viewed as the end-member of the series: $R_3MX_2O_8$, $R_2MX_2O_8$, $RMX_2O_8$ and $MX_2O_8$, where $R$ are monovalent cations (Serezhkin *et al.*, 1987). $\alpha$-$ZrMo_2O_8$ has electrically neutral layers bonded together by van der Waals forces between the oxygen pointing into the interlayer space and its closest neighbours, while the other members of the series have $R$ cations in-between the layers.

This study was performed as part of the high-pressure structural investigations on $MX_2O_8$ and $MX_2O_7$ compounds, and is an example of the possibility to use synchrotron X-ray powder diffraction data in combination with high-pressure cells to solve and refine a new complex framework structure.

## 2. Experimental

### 2.1. Sample preparation

Powder samples of trigonal $\alpha$-$ZrMo_2O_8$ were prepared by dehydrating a basic zirconium molybdate hydrate ($ZrMo_2O_7(OH)_2(H_2O)_2$), prepared essentially according to Clearfield & Blessing (1972). Aqueous solutions of the reactants, 20 ml of 0.5 *M* $ZrOCl_2{\cdot}H_2O$ and 20 ml of 1 *M* $Na_2MoO_4{\cdot}H_2O$, were mixed by simultaneous dropwise addition to 10 ml of water under continuous stirring. The obtained gel was aged overnight in the mother liquor, with continuous stirring. The gel and mother liquor was then acidified with 50 ml of 6 *M* HCl. This mixture was then heated at reflux temperature for 7 d. The obtained solid was then isolated, washed with 1 *M* HCl and water, and finally air-dried. The X-ray powder pattern was identical to the pattern of $ZrMo_2O_7(OH)_2(H_2O)_2$ in the ICDD database (No. 27-0994). Trigonal $\alpha$-$ZrMo_2O_8$ was obtained by heating $ZrMo_2O_7(OH)_2(H_2O)_2$ to 723 K for 18 h in a platinum crucible in air. The product was quenched by rapid cooling to room temperature. X-ray powder patterns of the prepared sample were identical to the pattern previously published by Auray *et al.* (1987).

### 2.2. Synchrotron X-ray studies

The X-ray powder diffraction experiments were carried out at the high-pressure beamline ID30, European Synchrotron Radiation Facility (ESRF), Grenoble, France. X-rays from two phased undulators (35 and 40 mm length, ~16 mm gap) were monochromated using a water-cooled channel-cut Si(111) monochromator operated in a vacuum. The wavelength was determined to $\lambda$ = 0.4250 (5) Å from the absorption edge of Sn (29.195 keV; Bearden, 1967) and by subsequent iterative least-squares fitting of the wavelength and sample-to-detector distance to a diffraction pattern of Si. The X-ray beam was collimated down to 0.080 × 0.080 $mm^2$ with tungsten carbide slits. Images of the powder diffraction rings were collected with an image-plate detector (Thoms *et al.*, 1998) of size 240 × 300 $mm^2$ (pixel size 0.07 × 0.08 $mm^2$) placed 500.00 (1) mm from the sample. The aperture of the high-pressure cell is restricted to 25° in 2$\theta$, giving a resolution of ~1 Å. The high-pressure cell was oscillated by ±3° perpendicular to the X-ray beam to increase the powder averaging.

Using the software *FIT2D* (Hammersley, 1998), the images were corrected for spatial distortion, non-linear features in the background, Lorenz factor and polarization before subsequent integration over the entire powder rings.

### 2.3. High-pressure technique

High pressure was applied using a membrane-driven diamond anvil cell equipped (Letoullec *et al.*, 1988) with 600 µm diameter diamond culets. A 4:1 methanol–ethanol mixture was added as the pressure medium. Stainless steel gaskets of 250 µm thickness were preindented down to 60–80 µm. The powder samples were loaded into the 250 µm diameter holes together with the pressure medium and a small ruby crystal (1–2 µm diameter spheres) close to the centre of the hole.

The ruby fluorescence technique (Piermarini *et al.*, 1975) was used to determine pressures by applying the calibration scale of Mao *et al.* (1986). Standard uncertainties (s.u.'s) were calculated from the precision in the readout of the wavelength shift and the reported errors in the pressure scale of 2% (Mao *et al.*, 1986). These s.u.'s are probably an underestimation of the error in the absolute pressure, but should reflect the precision in the relative change of pressure.

## 3. Results

There were 15 pressure points collected in the range 0.2–1.9 GPa. As mentioned above, the transition from $\alpha$- to $\delta$-$ZrMo_2O_8$ occurs at 1.06–1.11 GPa (Carlson & Krogh Andersen, 2000). The pressure-induced change in the diffraction pattern across the phase transition is illustrated in Fig. 1, on images of the complete powder rings for the $\alpha$- and $\delta$-phase at 0.32 and 1.64 GPa, respectively. These diffraction patterns and data extracted from them were chosen as examples of the structural characterization throughout this report. As can be seen, the powder in the pressure cell is of

excellent quality – visible single-crystal spots in the images are due to the ruby crystal (*cf.* above).

The new $\delta$-phase was indexed on the basis of the first 20 reflections in the diffraction pattern using the auto-indexing program *DICVOL*91 (Boultif & Louër, 1991). A monoclinic solution with a figure of merit $M(33) = 12$ (De Wolff, 1968) was suggested. The indexed powder pattern of $\delta$-$ZrMo_2O_8$ at 1.64 GPa is given in the supplementary material.[1] The systematic absences $h00$ ($h = 2n + 1$), $0k0$ ($k = 2n + 1$), $hk0$ ($h + k = 2n + 1$) and $h0l$ ($h = 2n + 1$) indicated that possible space groups could be *C*2, *Cm* or *C*2/*m* (*International Tables for Crystallography*, Vol. A, 1996). In the absence of any other indications, the highest symmetry [*C*2/*m* (No. 12)] was chosen. This choice of space-group symmetry was corroborated by the subsequent structural refinements.

The change of the unit-cell dimensions across the transition can be described by a transformation (Arnold, 1996) of the trigonal metric tensor (hexagonal setting) to pseudo-monoclinic symmetry (neglecting the monoclinic angle)

$$\mathbf{G}_\delta = \mathbf{P}^T \mathbf{G}_\alpha \mathbf{P},$$

where $\mathbf{G}_\alpha$ and $\mathbf{G}_\delta$ are the metric tensors for the trigonal and monoclinic phases, respectively. The transformation matrix $\mathbf{P}$ becomes

$$\mathbf{P} = \begin{pmatrix} -1/3^{1/2} & 1/3^{1/2} & 0 \\ 1/3^{1/2} & 1/3^{1/2} & 0 \\ 0 & 0 & 0.5 \end{pmatrix}.$$

Transformation from monoclinic to trigonal setting, including the monoclinic angle, can be performed by the expressions

$$a_\alpha = a_\delta$$

$$b_\alpha = 2(3)^{1/2} \cdot b_\delta$$

$$c_\alpha = 2 \sin \beta_\delta \cdot c_\delta.$$

The positions of all the atoms in $\delta$-$ZrMo_2O_8$ were found using direct methods on extracted intensities in the range $3 \leq 2\theta \leq 22^\circ$ with the software *EXPO* (Altomare *et al.*, 1999). Although the initial structure proposed by *EXPO* had already an *R* value of 0.126, the structure still included a number of wrong oxygen positions. These were easily corrected by inspection of bond distances and angles.

Rietveld refinements (Rietveld, 1969) of the structural models $\alpha$- and $\delta$-$ZrMo_2O_8$ against the collected high-pressure data were performed using the software *GSAS* (Larson & Von Dreele, 1994). Prior to the refinements the raw intensity data were converted from a simple $2\theta$ intensity format (floating point numbers; CHI-format) given by the *FIT*2*D* program, to the integer format of intensities for input in *GSAS* by a conversion program (Levy, 1999). A total of 14 refinements was performed. The results are listed in the supplementary material (all powder profiles with details are also given in the CIF file). Data at one pressure (1.1 GPa) in the transition could not be fully refined due to the mixing of the two phases. All refinements were performed with ~50 parameters, including scale factor, shifted-Chebyshev background parameters and pseudo-Voigt profile parameters. Details for two representative examples of the high-pressure refinements of the $\alpha$- and $\delta$-phase (0.32 and 1.64 GPa) are given in Table 1, and their respective difference plots are shown in Fig. 2. As can be seen in Table 1 and Fig. 2, the fits are remarkably good.

**Table 1**
Details of the high-pressure Rietveld refinements of $\alpha$-$ZrMo_2O_8$ (0.32 GPa) and $\delta$-$ZrMo_2O_8$ (1.64 GPa).

| Phase | $\alpha$-$ZrMo_2O_8$ | $\delta$-$ZrMo_2O_8$ |
|---|---|---|
| Pressure (GPa) | 0.32 (2) | 1.64 (3) |
| Temperature (K) | 298 | 298 |
| Crystal system | Trigonal | Monoclinic |
| Space group | $P\bar{3}c$ (No. 163) | *C*2/*m* (No. 12) |
| *a* (Å) | 10.14778 (9) | 9.7966 (3) |
| *b* (Å) | 10.14778 (9) | 5.98422 (17) |
| *c* (Å) | 11.6780 (2) | 5.28547 (18) |
| $\beta$ (°) | 90 | 93.069 (2) |
| *V* (Å$^3$) | 1041.46 (2) | 309.42 (2) |
| *Z* | 6 | 2 |
| $d_{calc}$ (g cm$^{-3}$) | 3.929 | 4.412 |
| $\lambda$ (Å) | 0.4250 (5) | 0.4250 (5) |
| $\mu$ (mm$^{-1}$) | 5.03 | 5.64 |
| No. of data | 2276 | 2011 |
| No. of observed reflections† | 346 | 153 |
| No. of parameters | 51 | 50 |
| $R_p$‡ | 0.006 | 0.006 |
| $wR_p$§ | 0.009 | 0.010 |
| $R_{F^2}$¶ | 0.033 | 0.046 |
| $\chi^2$†† | 1.30 | 2.85 |

† $I_o \geq 1 \cdot \sigma_I$. ‡ $R_p = \Sigma|y_i(\text{obs}) - y_i(\text{calc})|/\Sigma|y_i(\text{obs})$. § $wR_p = (\Sigma w_i[y_i(\text{obs}) - y_i(\text{calc})^2/\Sigma w_i[y_i(\text{obs})]^2)^{1/2}$. ¶ $R_{F^2} = \Sigma|F_{hkl}(\text{obs})^2 - F_{hkl}(\text{calc})^2|/|F_{hkl}(\text{obs})^2$. †† $\chi^2 = (\Sigma w_i[y_i(\text{obs}) - y_i(\text{calc})]^2/N_{\text{obs}} - N_{\text{var}}$.

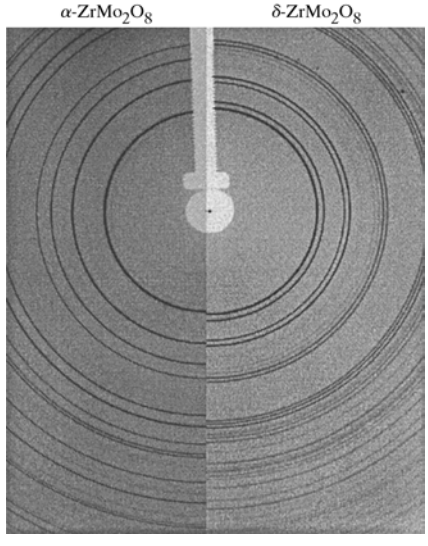


**Figure 1**
Diffraction patterns of $ZrMo_2O_8$ before (left, 0.32 GPa) and after (right, 1.64 GPa) the high-pressure transformation at 1.06–1.11 GPa. The light formation in the middle of the powder rings is the direct beam-stop. The single-crystal spot in the upper-right corner is due to the ruby crystal inserted for pressure measurements.

[1] Supplementary data for this paper are available from the IUCr electronic archives (Reference: SN0004). Services for accessing these data are described at the back of the journal.

**Table 2**
Fractional coordinates for $\alpha$-$ZrMo_2O_8$ at 0.32 (2) GPa.

Standard uncertainties (s.u.'s) are given in parentheses.

| Atom | *x* | y | z | $U_{iso}$ |
|---|---|---|---|---|
| Zr1 | 0 | 0 | 0 | 0.0021 (14) |
| Zr2 | 1/3 | 2/3 | 0.9752 (4) | 0.0021 (14) |
| Mo | 0.3298 (13) | 0.3375 (13) | 0.14778 (16) | 0.0137 (8) |
| O1 | 0.160 (5) | 0.150 (6) | 0.097 (2) | 0.005 (2) |
| O2 | 0.334 (7) | 0.506 (5) | 0.0923 (18) | 0.005 (2) |
| O3 | 0.523 (3) | 0.352 (4) | 0.1299 (14) | 0.005 (2) |
| O4 | 0.317 (5) | 0.345 (5) | 0.2909 (7) | 0.005 (2) |

**Table 3**
Fractional coordinates for $\delta$-$ZrMo_2O_8$ at 1.64 (3) GPa.

Standard uncertainties (s.u.'s) are given in parentheses.

| Atom | *x* | *y* | *z* | $U_{iso}$ |
|---|---|---|---|---|
| Zr | 0 | 0 | 0 | 0.017 (3) |
| Mo | 0.3300 (5) | 0 | 0.3119 (7) | 0.0098 (16) |
| O1 | 0.1121 (2) | −0.246 (2) | 0.849 (2) | 0.002 (3) |
| O2 | 0.1336 (13) | 0 | 0.2576 (20) | 0.002 (3) |
| O3 | 0.3730 (12) | 0 | 0.609 (2) | 0.002 (3) |

Resulting fractional coordinates from the Rietveld refinements for the $\alpha$- and $\delta$-phase at 0.32 and 1.64 GPa, respectively, are given in Tables 2 and 3. Bonding distances and angles calculated using the program *PLATON* (Spek, 1990) for the two refinements are given in Table 4, and for the entire pressure range in the supplementary material.

## 4. Discussion

In the pressure range investigated, and within experimental errors, the variation of the unit-cell parameters is linear (Fig. 3). Thus, a simple linear function may be used to describe the response of the structure to applied pressure. In general, the compressibility ($\beta$) of the unit-cell volume or axis length ($l$) can be defined as (Nye, 1985)

$$\beta_l = -(1/l)(\delta l/\delta p).$$

The limited accuracy of the pressure determination does not allow for higher-order fits of the compressibilities. Nevertheless, a linear description over this small pressure range is useful for interpolation and comparison with similar materials. The transition from $\alpha$- to $\delta$-$ZrMo_2O_8$ involves a discontinuity of 5% at 1.1 GPa (Fig. 3), and the volume compressibilities are 5.1 (1) $\times 10^{-2}$ and 4.2 (1) $\times 10^{-2}$ $GPa^{-1}$, respectively (Carlson & Krogh Andersen, 2000). This is 4–5 times higher than the value for the similar compound $\alpha$-$ZrW_2O_8$ (Jorgensen *et al.*, 1999). In fact, the compressibility of $ZrMo_2O_8$ is comparable to $ZrW_2O_8$ after 2.0–2.5 GPa [1.1 (1) $\times 10^{-2}$ $GPa^{-1}$], *i.e.* when it adopts the $\varepsilon$-$ZrMo_2O_8$ structure. In Fig. 3, the change in unit-cell parameters *versus* pressure over the transition can be seen. The *a* axis of the $\alpha$-phase with $\beta_a$ = 0.3 (1) $\times 10^{-2}$ $GPa^{-1}$ splits into the *a* and *b* axes with compressibilities of 1.5 (1) $\times 10^{-2}$ and −0.3 (1) $\times 10^{-2}$ $GPa^{-1}$, respectively. The compression of the *c* axes of the two phases remain similar over the transition with $\beta_c(\alpha)$ = 4.3 (1) $\times 10^{-2}$ $GPa^{-1}$ and $\beta_c(\delta)$ = 3.1 (1) $\times 10^{-2}$ $GPa^{-1}$. The larger compressibility in the *c*

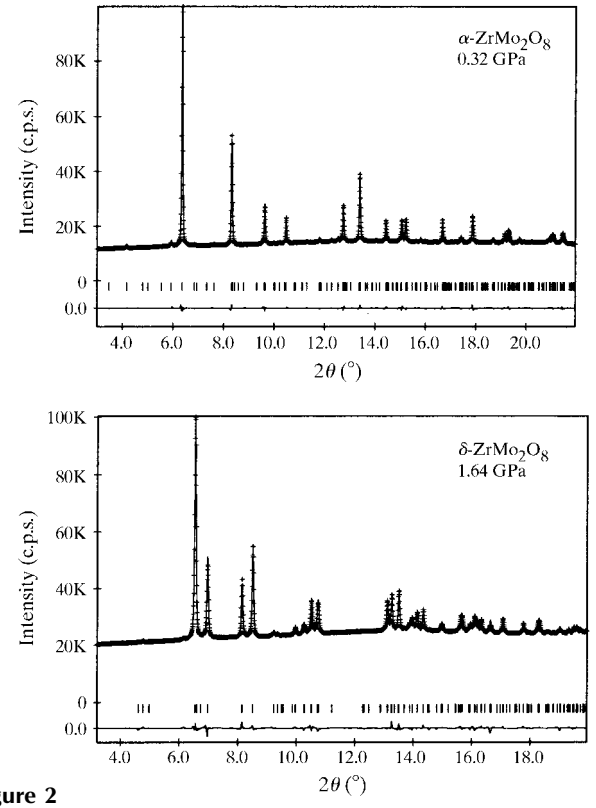


**Figure 2**
Observed (+) and calculated (−) profiles for Rietveld refinement of $\alpha$- and $\delta$-$ZrMo_2O_8$ at 0.32 and 1.64 GPa, respectively. The bottom curve is the difference plot and tick marks represent the allowed Bragg peak positions.

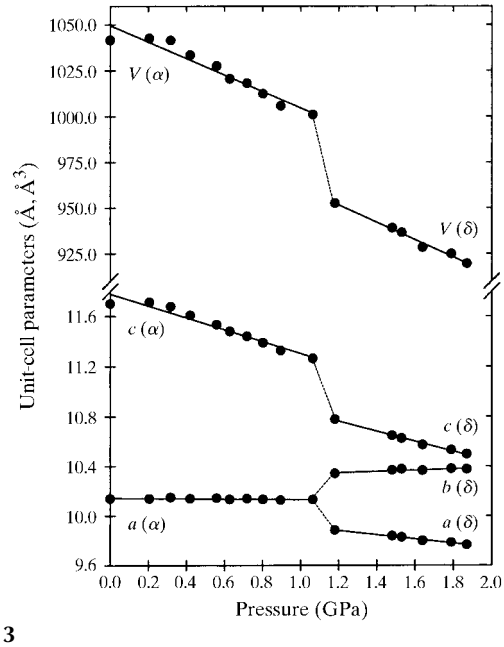


**Figure 3**
The change in unit-cell parameters for $\alpha$- and $\delta$-$ZrMo_2O_8$ up to 1.87 GPa. Transformation according to $b_\alpha = 2(3)^{1/2} \cdot b_\delta$ and $c_\alpha = 2 \sin b_\delta \cdot c_\delta$ for the monoclinic axes were performed to relate the axes of the $\delta$ with the $\alpha$ phase. Solid lines are merely guides for the eye.

direction of both phases is due to the connectivity of the structural elements into layers in the *ab* plane (Fig. 4), with only O4 from the $MoO_4$ groups pointing in-between the layers. Thus, most of the pressure increase is accommodated by simply decreasing the interlayer distance.

As can be seen in Fig. 4, compression of the layers in the *ab* plane is accomplished mainly by tilting of the $ZrO_6$ (dark octahedra) and $MoO_4$ (light tetrahedra) polyhedra. The layers formed by connecting the polyhedra in the *ab* plane of the structure shift slightly relative to each other across the transition at 1.1 GPa (right part, Fig. 4) to form the monoclinic angle 93°. A more detailed illustration of the displacive changes over the transition is given in Fig. 5, where a $Zr_2Mo_2O_{16}$ fragment viewed along the *c* axis is shown. The mapping of atoms between the $\alpha$- and $\delta$-phases can be seen from the assignment of atomic labels in the figure. Over the transition, the terminal O4 of the $\alpha$-phase transforms into O3 in the $\delta$-phase, becoming more or less parallel to the *c* axis. This is a displacement of ∼0.6 Å, while the corresponding decrease of the Mo—O bonding distance (Table 4) is 0.08 Å. For *e.g.* O1 bonded to Zr in the $\alpha$-phase, which transforms into O2 in the $\delta$-phase (Fig. 5), the displacement and change of the Zr—O distance over the transition are ∼0.3 and 0.1 Å, respectively. Thus, the displacive movements of the anions are greater than the compression of the Zr—O and Mo—O distances, implying that the $\alpha$-phase accommodates the applied pressure by improving the packing of its atoms.

In Table 4 selected distances and angles in the $\alpha$- and $\delta$-phases at 0.32 and 1.64 GPa are given. The Zr—O2 distances decrease by almost 0.2 Å over the transition, while the

**Table 4**
Selected bonding distances (Å), angles (°) and polyhedral volumes (Å$^3$) for the structures of $\alpha$- and $\delta$-$ZrMo_2O_8$.

Standard uncertainties (s.u.'s) are given in parentheses.

| $\alpha$-$ZrMo_2O_8$ | 0.32 (2) GPa | $\delta$-$ZrMo_2O_8$ | 1.64 (3) GPa |
|---|---|---|---|
| $Zr1-O1^{i,ii,iii,iv,v}$ | 1.94 (4)×6 | $Zr^{vi}-O1^{iii,vii,viii}$ | 2.023 (11)×4 |
| $Zr2^{ix}-O2^{x,xi}$ | 2.12 (4)×3 | $Zr^{vi}-O2^{vii}$ | 1.834 (12)×2 |
| $Zr2^{ix}-O3^{x,xi}$ | 1.99 (3)×3 | | |
| Mo—O1 | 1.91 (5) | $Mo-O1^{xii}$ | 1.846 (12)×2 |
| Mo—O2 | 1.82 (4) | $Mo-O2^{xiii}$ | 1.934 (14) |
| $Mo-O3^{xiv}$ | 1.90 (4) | Mo—O3 | 1.606 (11) |
| Mo—O4 | 1.681 (9) | | |
| $O1^{i,iii,iv}-Zr1-O1^{i,ii,iv,v}$ | 89 (2)×6 | $O1^{iii}-Zr^{vi}-O1^{vii,viii}$ | 86.6 (4)×2 |
| $O1^{i,ii}-Zr1-O1^{iii,iv,v}$ | 91 (2)×6 | $O1^{vii}-Zr^{vi}-O1^{iii,viii}$ | 93.4 (4)×2 |
| $O1^{i,ii}-Zr1-O1^{iii,iv,v}$ | 180 (3)×3 | $O1^{vii}-Zr^{vi}-O1^{iii,viii}$ | 180 (2)×2 |
| $O2^{x}-Zr2^{ix}-O2^{x,xi}$ | 83 (2)×3 | $O1^{iii,vii,viii}-Zr^{vi}-O2^{vii}$ | 85.2 (4)×4 |
| $O2^{x,xi}-Zr2^{ix}-O3^{x,xi}$ | 92.4 (18)×3 | $O1^{iii,vii,viii}-Zr^{vi}-O2^{vii}$ | 94.8 (4)×4 |
| $O2^{x,xi}-Zr2^{ix}-O3^{xi}$ | 98.9 (15)×3 | $O2-Zr^{vi}-O2^{vii}$ | 180 (2) |
| $O2^{x,xi}-Zr2^{ix}-O3^{x,xi}$ | 174.8 (19)×3 | | |
| $O3^{x}-Zr2-O3^{x,xi}$ | 85.9 (11)×3 | | |
| O1—Mo—O2 | 114 (2) | $O1-Mo-O1^{xii}$ | 110.9 (5) |
| $O1-Mo-O3^{xiv}$ | 115.0 (19) | $O1^{xii}-Mo-O2^{xiii}$ | 105.3 (4)×2 |
| O1—Mo—O4 | 107.5 (19) | $O1^{xii}-Mo-O3$ | 112.0 (4)×2 |
| $O2-Mo-O3^{xiv}$ | 111 (2) | $O2^{xiii}-Mo-O3$ | 111.0 (5) |
| O2—Mo—O4 | 106.2 (19) | | |
| $O3^{xiv}-Mo-O4$ | 102 (2) | | |
| Zr1—O1—Mo | 160.9 (19) | $Zr-O1^{xv}-Mo$ | 165.6 (6) |
| Zr2—O2—Mo | 160.7 (16) | $Zr-O2^{xv}-Mo^{xv}$ | 140.9 (6) |
| $Zr2-O3^{xiv}-Mo^{xiv}$ | 146.9 (10) | | |
| $V_{poly}(Zr1O_6)$ | 9.8 (3) | $V_{poly}(ZrO_6)$ | 9.90 (7) |
| $V_{poly}(Zr2O_6)$ | 11.4 (2) | | |
| $V_{poly}(MoO_4)$ | 3.07 (8) | $V_{poly}(ZrO_6)$ | 3.02 (3) |

(i) $-y, x-y, z$; (ii) $-x+y, -x, z$; (iii) $-x, -y, -z$; (iv) $y, -x+y, -z$; (v) $x-y, x, -z$; (vi) $\frac{1}{2}+x, \frac{1}{2}+y, z$; (vii) $-x, y, -z$; (viii) $x, 1-y, z$; (ix) $x, y, z-1$; (x) $1-y, 1+x-y, z$; (xi) $-x+y, 1-x, z$; (xii) $x, -y, z$; (xiii) $\frac{1}{2}-x, -\frac{1}{2}+y, -z$; (xiv) $1-x, 1-y, -z$; (xv) $\frac{1}{2}-x, \frac{1}{2}+y, -z$.

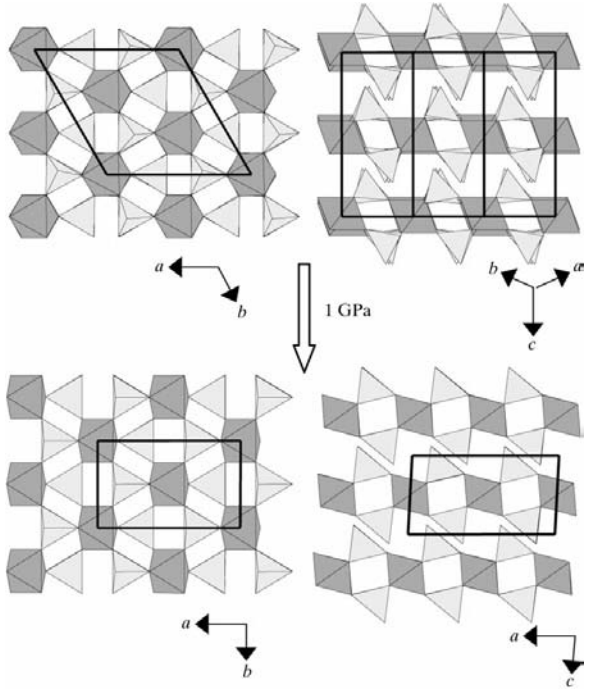


**Figure 4**
Illustration of the change of $ZrMo_2O_8$ over the transition at 1.06–1.11 GPa. Dark octahedra and light tetrahedra represent the $ZrO_6$ and $MoO_4$ coordination polyhedra, respectively.

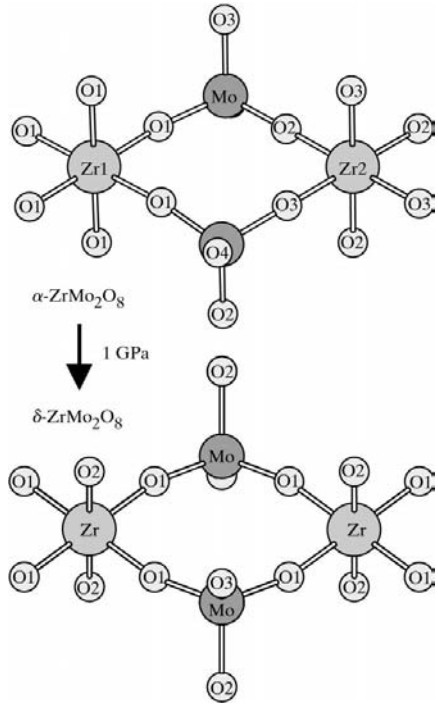


**Figure 5**
Detailed illustration of the changes of the $ZrO_6$ and $MoO_4$ connectivity (with atoms labelled for clarity) over the transition at 1.06–1.11 GPa for $ZrMo_2O_8$.

changes in Mo—O distances are more subtle. The distortion of the $ZrO_6$ octahedra is most clearly seen by the increasing deviation from ideal 90° for the O1—Zr—O1 angles. From being close to 90° in the $\alpha$-phase they become 86.6 and 93.4° in the $\delta$-phase. From the change in Zr—O—Mo angles (Table 4) the tilting of the polyhedra can be calculated to be 5–6°. The change in bonding distances and Zr—O—Mo angles with applied pressure for the entire experimental range (Fig. 6) are quite complex below the transition, while a simpler behaviour is observed for the $\delta$-phase.

A convenient way of describing the compression of structural elements such as $ZrO_6$ and $MoO_4$ is to calculate polyhedral volumes (Finger, 1971). The calculated polyhedral volumes *versus* pressure in Fig. 7 show that the volumes of the $ZrO_6$ octahedra and $MoO_4$ tetrahedra do not change much over the transition at 1.1 GPa. However, it can be seen from Fig. 7 that the parabolic behaviour of the polyhedral volumes change to a more linear pattern after the phase transition. It is also interesting to note that the polyhedral volume changes show a self-compensating effect within the structure to accommodate the increased pressure. For instance, in the $\alpha$-phase, the decrease of the $ZrO_6$ volumes is accompanied with a slight increase in the $MoO_4$ volume. After the transition this effect has disappeared and the volumes change linearly with pressure. Thus, as would be expected, the $\alpha$-phase is more loosely packed and open for the anions to move, while the $\delta$-phase is more close packed with the anion–anion repulsion forces governing the compression of the structure.

From the above descriptive details of the structural changes the major reason for the trigonal to monoclinic transition may be evaluated. As can be seen in Fig. 4, the structure appears to become more symmetric over the phase transition. This is mainly due to the more effective packing of the anions with applied pressure, shown schematically along the *c* axis in Fig. 8. The O atoms in Fig. 8 have been depicted at 0.32 and 1.64 GPa using a radius of half the distance to its nearest neighbouring anion, and the O atoms pointing into the interlayer space (O4 and O3 for the $\alpha$- and $\delta$-phase, respectively) are marked with a dark shading. The less effective packing of anions for the $\alpha$-phase result in higher compressibility and fairly complicated pressure-induced changes for structural properties, such as bonding distances and angles (Fig. 6). After the transition, when more effective packing is achieved for the anions, the compressibility decreases and changes in structural properties are more or less linear with pressure. By viewing the structure as composed of hard spheres of similar size it would perhaps ideally go from trigonal to a higher symmetry, but since the structure has atoms of different sizes it has to find the best compromise for the packing. Thus, the *a*–*b* layers of the $\alpha$-phase have to shift slightly to achieve the most effective packing of all the constituent atoms, which results in a monoclinic angle of ~93°.

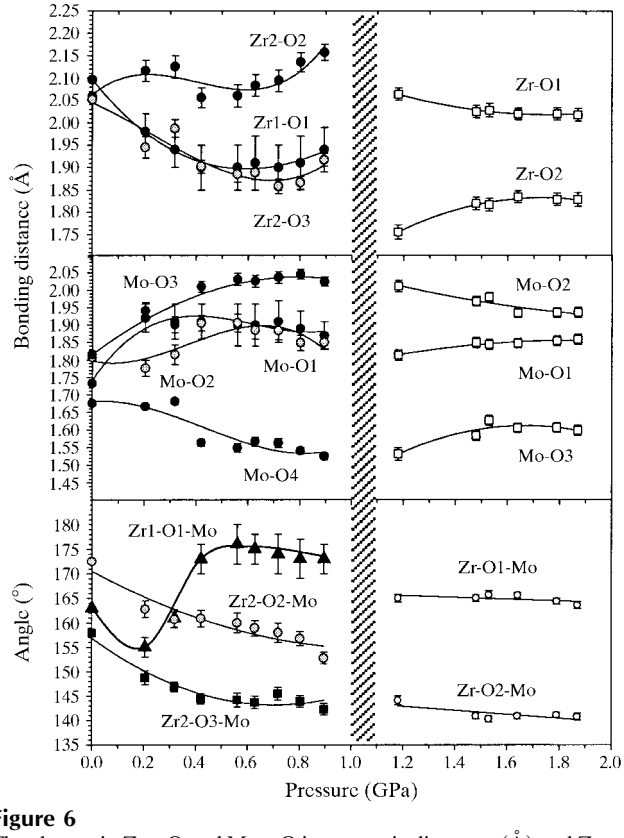


**Figure 6**
The change in Zr—O and Mo—O interatomic distances (Å) and Zr—O—Mo angles (°) for $\alpha$- and $\delta$-$ZrMo_2O_8$. Solid lines are merely guides for the eye. Room-pressure data are taken from Auray *et al.* (1986).

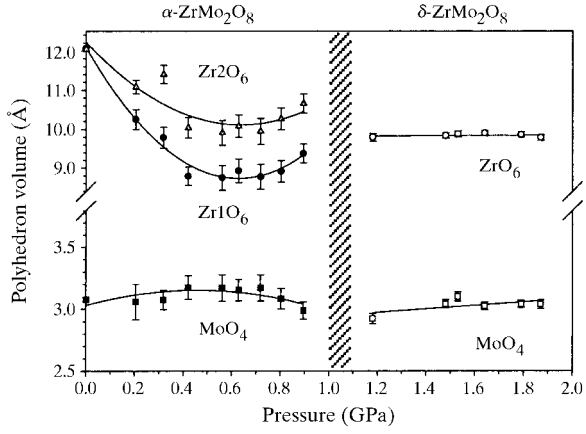


**Figure 7**
Calculated polyhedral volumes (Å$^3$) *versus* pressure for $\alpha$- and $\delta$-$ZrMo_2O_8$. Room-pressure data are taken from Auray *et al.* (1986).

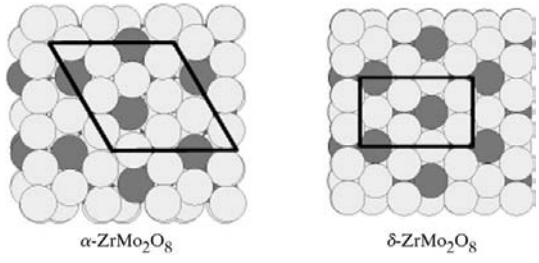


**Figure 8**
The change in packing of anions over the transition at 1.06–1.11 GPa for $ZrMo_2O_8$, viewed along the *c* axis. The dark spheres represent the terminal $MoO_4$ oxygen pointing into the interlayer (O4 and O3 for the $\alpha$- and $\delta$-phase, respectively), while light spheres are the remaining O atoms.

## 5. Conclusions

The structure determination of $\delta$-$ZrMo_2O_8$, stable between 1.1 and 2.5 GPa, has been performed from high-pressure synchrotron X-ray powder diffraction data. The $\alpha$–$\delta$ transition at 1.06–1.11 GPa is shown to be driven by the change in packing of the anions to a more dense arrangement. The second high-pressure transition from $\delta$- to triclinic $\varepsilon$-$ZrMo_2O_8$ occurs at 2.5 GPa (Carlson & Krogh Andersen, 2000). Considering the large unit-cell volume decrease of 10% in the $\delta$–$\varepsilon$ transition, it seems reasonable that packing effects are also the major reason for this transition. More investigations on the triclinic $\varepsilon$-phase is currently in progress.

## References


Adachi, T., Muromura, T., Takeshi, H. & Yamamoto, T. (1988). *J. Nucl. Mater.* **160**, 81–87.

Altomare, A., Burla, M. C., Camalli, M., Carrozzini, B., Cascarano, G. L., Giacovazzo, C., Guagliardi, A., Moliterni, A. G. G., Polidori, G. & Rizzi, R. (1999). *J. Appl. Cryst.* **32**, 339–340.

Arnold, H. (1996). *International Tables for Crystallography*, Vol. A, pp. 70–75. Dordrecht, The Netherlands: Kluwer Academic Publishers.

Auray, M., Quarton, M. & Tarte, P. (1986). *Acta Cryst.* C**42**, 257–259.

Auray, M., Quarton, M. & Tarte, P. (1987). *Powder Diffr.* **2**, 36–38.

Auray, M., Quarton, M. & Tarte, P. (1989). *Powder Diffr.* **4**, 29–30.

Bearden, J. A. (1967). *Rev. Mod. Phys.* **39**, 78–124.

Blasse, G. & Dirksen, G. J. (1987). *J. Phys. Chem. Solids*, **48**, 591–592.

Boultif, A. & Louër, D. (1991). *J. Appl. Cryst.* **24**, 987–993.

Carlson, S. & Krogh Andersen, A. M. (2000). *Phys. Rev. B*, **61**, 11209–11212.

Chu, C. N., Saka, N. & Suh, N. P (1987). *Mater. Sci. Eng.* **95**, 303–308.

Clearfield, A. & Blessing, R. H. (1972). *J. Inorg. Nucl. Chem.* **34**, 2643–2663.

Evans, J. S. O., Hu, Z., Jorgensen, J. D., Argyriou, D. N., Short, S. & Sleight, A. W. (1997). *Science*, **275**, 61–65.

Evans, J. S. O., Mary, T. A., Vogt, T., Subramanian, M. A. & Sleight, A. W. (1996). *Chem. Mater.* **8**, 2809–2823.

Finger, L. W. (1971). *VOLCAL.* Carnegie Institution of Washington, Geophysical Laboratory, Washington DC.

Hammersley, A. (1998). *FIT2D*, Version 10.3, Reference Manual Version 4.0. ESRF, Grenoble, France.

Jorgensen, J. D., Hu, Z., Teslic, S., Argyriou, D. N., Short, S., Evans, J. S. O. & Sleight, A. W. (1999). *Phys. Rev. B*, **59**, 215–225.

Klevtsova, R. F., Glinskaya, L. A., Zolotova, E. S. & Klevtsov, P. V. (1989). *Dokl. Akad. Nauk. SSSR*, **305**, 91–95.

Korthuis, V., Khosrovani, N., Sleight, A. W., Roberts, N., Dupree, R. & Waren, W. W. (1995). *Chem. Mater.* **7**, 412–417.

Larson, A. C. & Von Dreele, R. B. (1994). *LANSCE MS-H*805. Los Alamos National Laboratory, Los Alamos, USA.

Letoullec, R., Pinceaux, J. P. & Loubeyre, P. (1988). *High Press. Res.* **1**, 77–96.

Levy, D. (1999). *CHI2GSAS.* ESRF, Grenoble, France.

Lind, C., Wilkinson, A. P., Hu, Z., Short, S. & Jorgensen, J. D. (1998). *Chem. Mater.* **10**, 2335–2337.

Mao, H. K., Xu, J. & Bell, P. M. (1986). *J. Geophys. Res.* **91**, 4673–4676.

Mary, T. A., Evans, J. S. O., Vogt, T. & Sleight, A. W. (1996). *Science*, **272**, 90–92.

Mittal, R., Chaplot, S. L., Lalla, N. P. & Mishra, R. K. (1999). *J. Appl. Cryst.* **32**, 1010–1011.

Moore, P. B. (1973). *Am. Mineral.* **58**, 32–42.

Nye, J. F. (1985). *Physical Properties of Crystals*, pp. 145–146. Oxford University Press.

Pankajavalli, R. & Sreedharan, O. M. (1990). *J. Nucl. Mater.* **172**, 151–154.

Perottoni, C. A. & Jordana, J. A. H. (1998). *Science*, **280**, 886–889.

Piermarini, G. J., Block, S., Barnett, J. D. & Forman, R. A. (1975). *J. Appl. Phys.* **46**, 2774–2780.

Prinetto, F., Cerrato, G., Ghiotti, G., Chiorino, A., Campa, M. C., Gazzoli, D. & Indovina, V. (1995). *J. Phys. Chem.* **99**, 5556–5567.

Rietveld, H. M. (1969). *J. Appl. Cryst.* **2**, 65–71.

Rimsky, A., Thoret, J. & Freundlich, W. (1968). *Comp. R. Acad. Sci. Paris Ser. C*, **267**, 1468–1470.

Serezhkin, V. N., Efremov, V. A. & Trunov, V. K. (1987). *Russ. J. Inorg. Chem.* **32**, 1566–1570.

Spek, A. L. (1990). *PLATON.* University of Utrecht, The Netherlands.

Thoms, M., Bachau, S., Häusermann, D., Kunz, M., Le Bihan, T., Mezouar M. & Strawbridge, D. (1998). *Nucl. Instrum. Methods Phys. Res. A*, **413**, 175–184.

Wolff, P. M. de (1968). *J. Appl. Cryst.* **5**, 108–113.